Nuclear Science and Techniques (2025) 36:92
https://doi.org/10.1007/s41365-025-01677-5

Insights into the effects of oxygen content regulation on the microstructure and mechanical properties of in situ ODS 304 L stainless steel processed by laser powder bed fusion

Yan-Lin Gu[1] · Fan Yang[1] · Yu-Yu Guo[1] · Zhen Yan[1] · Ai-Jun Huang[2] · Juan Hou[1]

Received: 9 March 2024 / Revised: 18 June 2024 / Accepted: 19 June 2024 / Published online: 17 April 2025

Abstract

Laser powder bed fusion (LPBF) is a widely used and well-developed approach in additive manufacturing. To meet the high material performance requirements of fourth-generation nuclear power reactors, the combination of LPBF processing with oxide dispersion strengthening (ODS) is currently of interest for the design and development of new materials. In this approach, nanoscale Y_2O_3 particles are dispersed into the feeding powders to produce LPBF-ODS materials. Oxygen exposure and the introduction of oxygen into the solvation cell during LPBF are usually considered as detrimental processes that are impossible to eliminate completely. However, our understanding of these unavoidable processes is still limited. In this study, we developed a new LPBF-ODS design approach based on in situ oxygen content regulation during the LPBF process. The oxygen content of the environmental chamber was artificially adjusted using an online monitoring system to activate reactions between oxygen and the metallic elements for the in situ formation of dispersed oxide particles. Four batches of LPBF 304 L stainless steel samples were successfully processed under different oxygen levels to investigate the reinforcement effect of in situ chemical alloying. The results show that dispersed oxide particles were formed with an average nanoscale size of approximately 46 nm through the LPBF in situ alloying approach. The increase in the number density of oxide particles to 11.4 particles /μm^2 as the oxygen content increased played a role in refining and stabilizing the cellular structure. The yield strength of the in situ alloyed ODS material was enhanced (to up to ~ 675 MPa) while its ductility was not significantly degraded (elongation of up to ~ 39%). These tensile properties are competitive within the ranges reported for ODS alloys prepared by mechanical alloying. The main mechanisms for yield strength enhancement through interactions between nanoscale oxide particles and dislocation entanglement cells were analyzed. This study provides a new approach for the future preparation of high-performance LPBF-ODS alloys.

Keywords ODS alloy · Laser powder bed fusion · Oxygen content · Mechanical properties

1 Introduction

Generation-IV (Gen-IV) nuclear power reactors provide safer and more sustainable, proliferation-resistant, and economically viable nuclear energy compared to previous reactors [1–3]. The primary requirements for the successful development and deployment of Gen-IV reactor systems are the performance and reliability of the structural materials in both nuclear and extranuclear applications [4]. Austenitic stainless steel (SS) is the material of first choice for reactor core components because of its excellent mechanical properties and resistance to corrosion and irradiation [5]. However, it has been observed that the irradiation endurance of traditionally manufactured austenitic SS, although significant,

This work was supported by the National Natural Science Foundation of China (Nos. U22B2067 and 52073176).

✉ Juan Hou
houjuan@usst.edu.cn

[1] School of Materials Science and Engineering, University of Shanghai for Science and Technology, Shanghai 200093, China

[2] Monash Centre for Additive Manufacturing, Monash University, Notting Hill, VIC 3168, Australia

may still fall short under the harsh irradiation conditions expected in future reactor technologies [1].

To improve the mechanical properties of structural materials for nuclear applications, several methods have been employed to prepare 304 L SS such as improvements in the molding process and composition optimization [6, 7]. Among these methods, the oxide particle dispersion strengthening of 304 L SS is the most promising method. This process involves the addition of nanoscale Y_2O_3 particles to the raw materials to overcome the material limits in high-temperature applications and improve irradiation resistance [8–10]. These improvements are achieved through the high density of thermally stable nano-oxide particles dispersed throughout the metal matrix. In recent years, several attempts have been made to disperse oxide particles within the material matrix using mechanical alloying (MA) and subsequently perform hot isostatic pressing to produce oxide dispersion-strengthened (ODS) alloys. However, these processes are time-consuming, challenging to scale up, produce nonuniformly distributed nano-oxide particles within the matrix, and highly susceptible to contamination [8, 11, 12]. Xu et al. [13] observed a significant reduction in the ductility of 304 L ODS SS from 41% to 19% due to impurity elements introduced during the MA process. This reduction may be attributed to the emergence of deformation cracks at the interfaces between the hard ceramic nano-oxide particles and weak metal matrix.

Laser powder bed fusion (LPBF), an additive manufacturing (AM) technique also known as selective laser melting (SLM), has gained popularity for the production of complicated components because it eliminates the need for time-consuming mold designs or additional machining processes [14]. The high cooling rates $\left(10^5 - 10^7\ \mathrm{K/s}\right)$, high-temperature gradients, and multiple heat cycles in the LPBF process produce a nonequilibrium microstructure. The microstructure has an ultrafine cellular structure containing δ ferrite, σ phase, and nano-oxide particles [15], which differs significantly from the microstructure of conventional austenitic 304 L SS. This unique microstructure can improve both material strength and ductility, and offers a promising route for fabricating components with unique mechanical properties compared to typical production procedures [8].

In LBPF, ball milling is utilized to mix material powders with oxide particle powders for the subsequent production of homogenous ODS alloys through layer-by-layer LPBF processing [15–17]. Ghayoor et al. [18] incorporated 5.1wt% Y_2O_3 into raw powders to fabricate SLM-ODS 304 L samples using SLM. They observed that the interactions between the Y_2O_3 particles and the honeycomb-like cellular substructure hindered dislocation and grain boundary migration. The yield strength (YS) and ultimate tensile strength (UTS) of the SLM-ODS material were improved to 575 MPa and 700 MPa, respectively. These values are superior to the previously reported values for SLM 304 L SS, which has a YS of only 540 MPa and UTS of 660 MPa [15]. However, the dopant particles reduced the material elongation (EL) from 36% to 32%.

These observations are similar to those reported by AlMangour [17], who investigated the addition of TiB_2 powder to 316 L followed by LPBF processing. The resultant improvements in the mechanical properties are attributed to nanoscale TiB_2, which limited grain growth and refined the grain sizes of the formed nanocomposites. However, the reduction in EL also exposes the limitations of LPBF-ODS materials prepared by oxide particle doping. The cracks and voids at the interface between the hard ceramic particles and metal matrix reduce material integrity. Furthermore, the uniform dispersion of particles within the material remains a challenge. In their pioneering work, Guo et al. [19] reported that the particle dispersion distribution was affected by the laser energy density and that a regular ring-like distribution along the metal grain boundaries appeared at high laser power. However, these findings were contradicted by Wang et al. [20], who reported that the reinforcing particles tended to be uniformly distributed when the laser power was increased in oxide dispersion-reinforced AI matrix composites. In addition, by using particles as melt flow tracers, Guo et al. [19] found that the particles tended to flow with the Marangoni vortex during the LPBF processes. These studies indicate that the potential mechanisms controlling the particle flow dynamics during LPBF are still unclear, and that improved methods for the uniform dispersion of nano-oxide particles remain to be explored.

The introduction of nano-oxide particles during LPBF has been shown to enhance the high-temperature tensile and creep properties of materials [21, 22]. Timothy et al. [21] reported a twofold increase in strength, thousand-fold improvement in creep properties, and twofold enhancement in oxidation resistance in GRX-810 with internally doped Y_2O_3 prepared by LPBF compared with its conventional counterpart at 1093 °C.

Jovid et al. [22] found that the presence of evenly distributed Y_2O_3 particles in LPBF Hastelloy X improved the resistance of the grain structure to recrystallization during dissolution and creep at high temperatures. Furthermore, the ODS alloy was more creep resistant at high stresses (from 50 MPa to 120 MPa) than the oxide-free alloy, as expected from the impeded dislocation motion due to the oxide dispersoids. It is therefore essential to refine LPBF-ODS to address the challenges related to the particle–matrix interface and nonuniform dispersion distribution to significantly enhance the mechanical properties of the material.

It was recently proposed that changing the oxygen content of the chamber during LPBF can be a new approach for preparing complex components with ODS structures. However, research on this approach is still limited, especially in terms

of in-depth studies on the effects of the oxygen content on the microstructure and mechanical properties. Hsu et al. [23] successfully prepared 17 − 4 PH SS enriched with nano-oxide particles by regulating the oxygen content to 500 ppm during SLM. An in situ chemical synthesis approach was adopted to form oxide particles. The yield strength was increased to 154.5 MPa with 62% of the increase attributed to nano-oxide strengthening and 38% to finer martensite encapsulation. Song et al. [24] investigated the effects of the environmental oxygen partial pressure on the morphology, composition, size, and number density of oxide inclusions in AISI 420 SS prepared using laser solid forming. They found that both the volume fraction and dimensions of the nano-oxide particles within the material increased with the oxygen content, and that larger nano-oxide particles were located at the boundaries of the cellular structure. This configuration was expected to improve the mechanical properties of the material by impeding plastic deformation. Deng et al. [14] studied the morphology and size of oxide inclusions formed by residual oxygen in LPBF 316 L SS as well as the changes in the chemical composition with the temperature and heat treatment time. Their results indicate that during recrystallization, grain boundary migration played a crucial role in oxide coarsening, leading to rapid growth in the early stages of recrystallization. In addition, at higher temperatures ($T > 1065\,^{\circ}C$), oxide coarsening was primarily controlled by lattice diffusion; however, grain boundary diffusion also contributed significantly through oxide-grain boundary interactions. The above studies suggest that although the preparation of LPBF-ODS alloys by oxygen content regulation is feasible, variations in the oxygen content can impact the oxide particles and affect material performance. However, our understanding of the microstructure and mechanical properties of LPBF-ODS materials is currently limited by the dearth of studies on the effects of oxygen content variations.

As mentioned previously, extensive research has been performed on enhancing the mechanical properties of LPBF SS through the introduction of diffusely and randomly distributed nano-oxide particles [25–29]. Previous studies have mainly focused on improving the raw materials and regulating the oxygen content in the process parameters to optimize the material properties. In contrast, the aim of our study is to investigate the impact of oxygen content variations on the oxide particles formed in situ during LPBF and their effects on the mechanical properties. Samples were prepared under a wide oxygen content range (50 ppm − 1500 ppm) to clarify the effects of increased oxygen on the oxide particles formed in situ.

2 Experiment

2.1 Sample preparation and LPBF process

The powder used in this study is gas-atomized 304 L SS powder with the elemental composition listed in Table 1. The particle sizes in the powder range from 10 µm to 53 µm.

The LPBF process was performed using a Hanbon HBD-150 machine in an argon-gas-protected environment under the optimized parameters of 160 W laser power, 1000 mm/s scanning speed, 75 µm scanning pitch, and 30 µm layer thickness. The scanning direction was rotated by 67° between adjacent layers. The horizontal samples were oriented parallel to the laser beam scanning plane (X-Y plane). To investigate the microstructure and mechanical properties at the different oxygen contents of (50 ppm, 500 ppm, 1000 ppm, and 1500 ppm), blocks with the dimensions of 45 mm × 15 mm × 15 mm and 15 mm × 15 mm × 15 mm were fabricated horizontally, as shown schematically in Fig. 1.

2.2 Mechanical performance evaluation

LPBF blocks were cut and machined into uniform flat-dogbone tensile specimens with a gauge length of 12 mm. The loading direction was normal to the building direction, as shown in Fig. 1. All the tensile experiments were performed using a 50 kN testing machine (Zwick Proline, Germany). The loading rate under displacement control mode was set to 0.5 mm/min. To minimize measurement errors, the average value was calculated for three specimens under the same test conditions. Prior to the tensile experiments, the surfaces of the samples were gradually polished using grit sandpaper from 180 to 3000 # to reduce static friction.

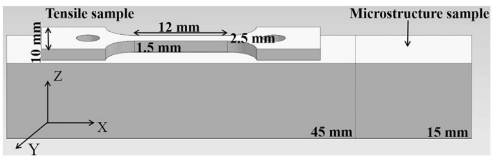

Fig. 1 (Color online) Schematic of tensile and microstructure specimens

Table 1 LPBF 304 L powder composition

Element	C	N	Si	Mn	Cu	Cr	Ni	Mo	Co
wt.%	0.014	0.013	0.065	0.054	0.032	19.07	9.62	0.83	0.016

2.3 Microstructural characterization

The microstructure and fracture morphology of LPBF 304 L SS after the room-temperature tensile test were characterized using a field-emission scanning electron microscope (FESEM, Zeiss Gemini SEM 300, Germany). Samples with horizontal surfaces for SEM observation were metallographically prepared using a 0.04 μm-colloidal silica finish. Electrochemical etching for electron microscopy observation was then performed at 5 V for 45 s in 10% oxalic acid solution. An energy-dispersive X-ray spectroscopy (EDS) spectrometer was used to perform elemental composition analysis on the oxides to provide comprehensive insight into their microstructural attributes.

Additionally, electron backscatter diffraction (EBSD) was performed to study the grain sizes, morphologies, and grain orientations of the fabricated specimens. To remove the surface deformation layer prior to the EBSD measurements, the specimens were polished to a mirror finish followed by electrochemical polishing with 10% $HClO_4$ and 90% C_2H_6O. EBSD data were collected at a step size of 0.5 μm, and post-analysis performed on the EBSD results using TSL OIM (version 8.6).

To characterize the nano-oxide particles and substructure of LPBF 304 L SS in detail, transmission electron microscopy (TEM) observations were conducted using an FEI Tecnai F30 at 200 kV. Prior to TEM analysis, the samples were shaped into small disk specimens (thickness: 50 μm, diameter: 3 mm) and the disks were further electropolished in 5 vol. % perchloric acid and 95 vol.% ethanol solution at −30°C and 30 V using a Struers twin-jet electropolisher. Thirteen TEM images of samples with each oxygen content level were meticulously analyzed using ImageJ (version 1.53) in conformance to the ASTM E1245 standard to elucidate the nano-oxide particle variations and proportions at different oxygen levels.

The phases and their fractions were identified using a D8 X-ray diffraction (XRD) system over a scan angle range of 30°–90° at a scan speed of 0.01%. The austenite phases in LPBF 304 L SS were identified based on JCPDS card 54-0331. The nano-oxide particles in LPBF 304 L SS were identified as SiO_2 based on JCPDS card 47-1144 and the TEM EDS results.

2.4 Theoretical material strength calculation

A finite element model was developed in ANSYS according to standard coding protocols using Mechanical APDL 2022R1. The model simulated a 1 μm^2 square region, within which oxide nanoparticles with a diameter of 46 nm were randomly distributed. The mechanical properties of the materials were simulated for the two distinct particle concentrations of 0.03% for the 50 ppm state and 0.07% for the 1500 ppm state. ANSYS APDL was utilized for mesh generation and constraint application. Mesh homogenization was performed to obtain an accurate equivalent homogeneous material to facilitate the subsequent simulations [30]. The boundary conditions were set such that the left side of the square area was fixed whereas the right side was subjected to stress to replicate the actual tensile experiment conditions.

The particle number density distributions were configured using APDL based on the experimental data. The theoretical YS values of the materials were calculated using the theoretical models. Material failure was studied by integrating the same displacements into the theoretical model. This approach effectively revealed the influence of the oxide particles on the elongation properties of the material to provide a clear and logical connection between theory and the experimental observations.

3 Results

3.1 Microstructural analysis

Figure 2 shows the XRD patterns of LPBF 304 L SS prepared under different oxygen content levels (50 ppm, 500 ppm, 1000 ppm, and 1500 ppm). Across these oxygen levels, sharp peaks corresponding to austenite with an FCC structure were detected. Austenite, which is denoted by black triangles, is the dominant phase. The subtle peak observed in the detailed scan range of 50° to 60° was identified as SiO_2 (PDF card 47–1144). In addition, the extensive variation in oxygen content did not result in an obvious new phase.

The SEM micrographs in Fig. 3a–d show the horizontal cross-sectional views of the post-electroetched LPBF 304 L SS samples. The detailed microstructural morphologies of these samples with oxygen contents ranging from 50ppm to 1500ppm in as-deposited conditions are captured in Fig. 3a1–d1. The cellular structures within the austenite grains delineated by the yellow boxes in Fig. 3a2–d2 indicate the presence of uniformly distributed ultrafine cellular substructures with dimensions of approximately 330 nm in all the samples, irrespective of their oxygen contents.

These samples exhibit a random distribution of numerous small nano-oxide particles, both within and at the boundaries of the cellular structure. Furthermore, a notable distortion was observed in the cellular structure of LPBF-ODS 304 L. The samples have a smaller cellular substructure than that of LPBF 304 L SS prepared by Hou et al. [15, 18], which are approximately 500 nm in size.

The higher magnification (50 kX) images of the base material in Fig. 3a3–d3 indicate the presence of numerous nano-oxide particles dispersed throughout the material. The concentration of these nano-oxide particles is positively correlated with the oxygen content. Their quantity

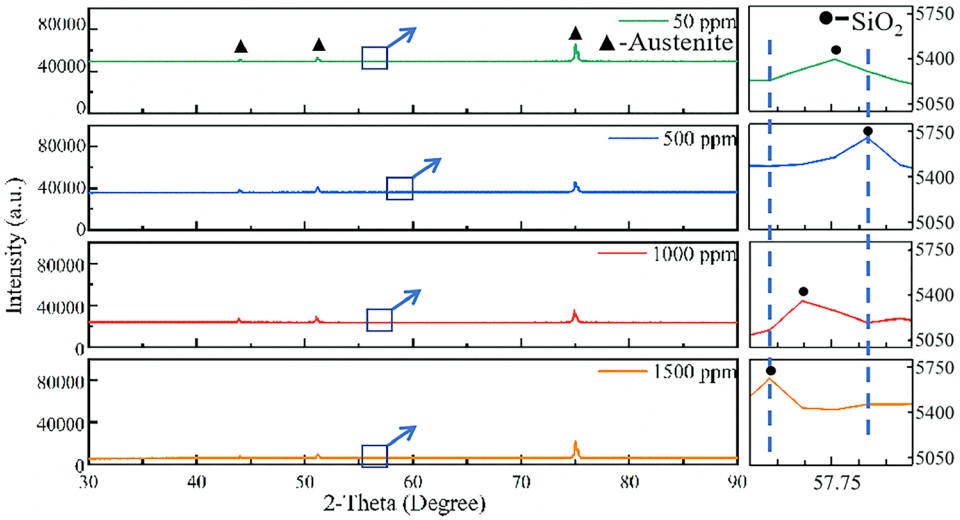

Fig. 2 (Color online) XRD phase identification patterns of samples with the four oxygen content levels

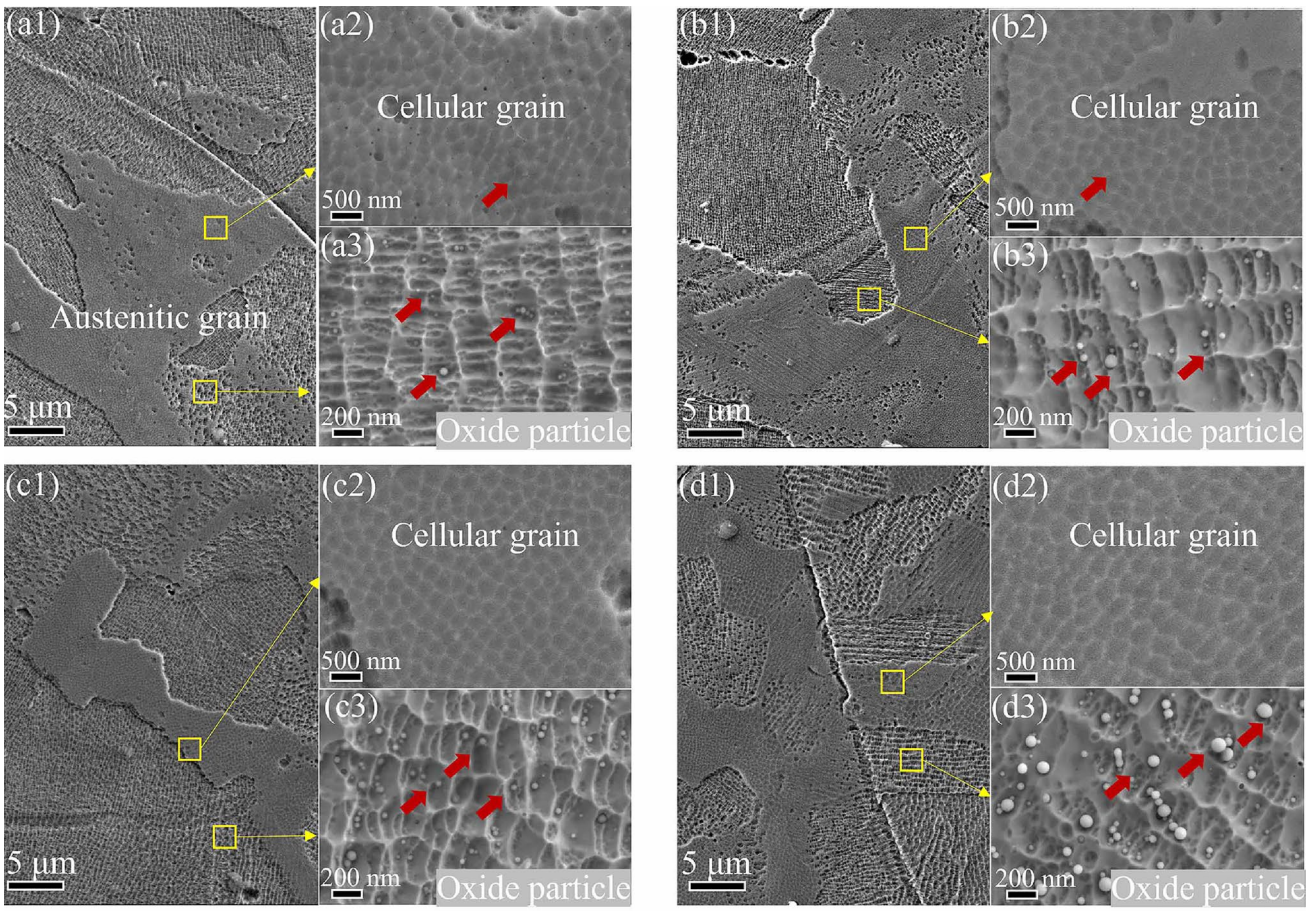

Fig. 3 (Color online) SEM images of cellular substructure and nano-oxide particles in as-built samples: (a) 50 ppm, (b) 500 ppm, (c) 1000 ppm, (d) 1500 ppm

and distribution are critical factors that affect the mechanical properties of the material, which will be discussed in Sects. 3.2 and 4.1. Notably, the nano-oxide particles are

significantly enriched under high-oxygen content conditions. This particle agglomeration is consistent with a similar particle enrichment observed in a previous study on LPBF 17 – 4 PH SS with 500 ppm oxygen content.

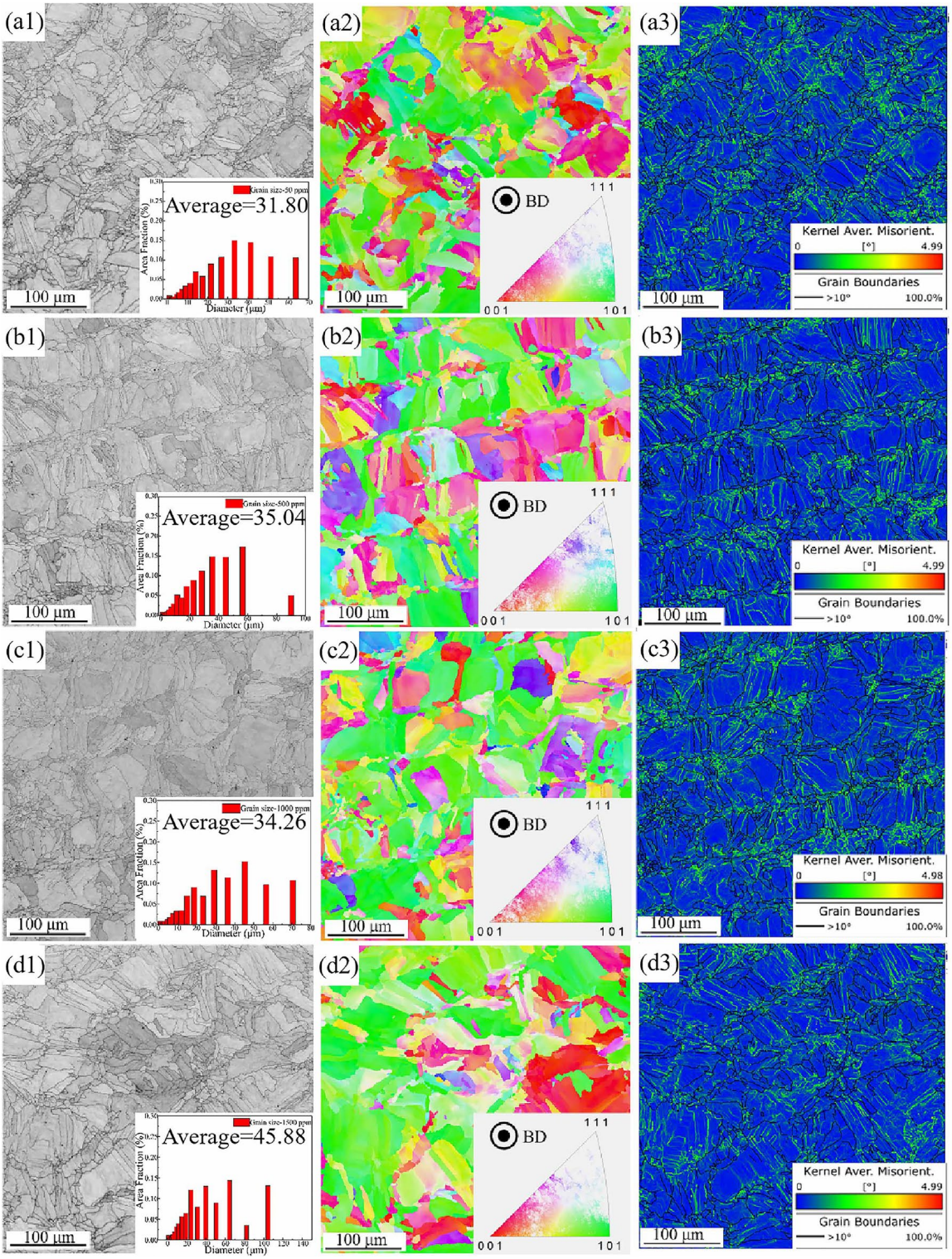

Fig. 4 (Color online) EBSD maps of LPBF 304 L ODS SS with oxygen contents of 50 ppm to 1500 ppm: (a1-d1) band contrast maps and grain size distribution statistics, (a2-d2) grain orientation maps with respect to building direction, (a3-d3) KAM maps of the four samples

The evolution of the LPBF 304 L SS microstructure with the oxygen content was further analyzed using EBSD. The results are shown in Fig. 4. The band contrast maps and grain size distributions across the four oxygen levels are presented in Fig. 4a1–d1 where the average grain sizes of the samples range from 31.80 µm at 50 ppm to 45.88 µm at 1500 ppm. There is a slight difference between the average grain sizes of the samples. It is noteworthy that the LPBF 304 L SS samples studied by Yang et al. [31] exhibited a markedly smaller average grain size of 10.41 µm, possibly because of the different printing parameters employed. The grain misorientation on the horizontal plane is shown in Fig. 4a2–d2, which show the grain orientation maps and their corresponding inverse pole figures (IPFs). The IPFs indicate that the misorientation of the austenite grains along the building direction is mainly concentrated along ⟨001⟩ and ⟨101⟩ with no obvious texture. Considering that the precipitates are too small to be accurately detected by EBSD, more in-depth analysis was carried out through TEM characterization subsequently. The kernel average misorientation (KAM) maps in Fig. 4a3–d3 quantify the average angular misorientation between a specific data point and its neighbors. They show that varying the oxygen content in the process parameters did not significantly influence the geometrically necessary dislocation (GND) densities within the as-deposited samples. These samples exhibit low overall stress levels without significant stress concentrations. It should be noted that the stress levels are increased along the melt pool boundaries. This increase is attributed to the elevated energy density and thermal cycling inherent in the printing process [8].

As mentioned previously, the oxide particles are extremely small and fall below the spatial resolution of SEM. SEM-based characterization methods such as EBSD therefore cannot provide a comprehensive picture of their properties. TEM bright-field (BF) images (Fig. 5a–d) were instead used to determine the precise distributions of the nano-oxide particles under oxygen contents ranging from 50 ppm to 1500 ppm. As shown in Fig. 5a1–d1, not only are these nano-oxide particles located along the boundaries and interiors of the cellular structures, but they also display two distinct contrasts. The brighter particles are termed the white particles, whereas those that appear darker are

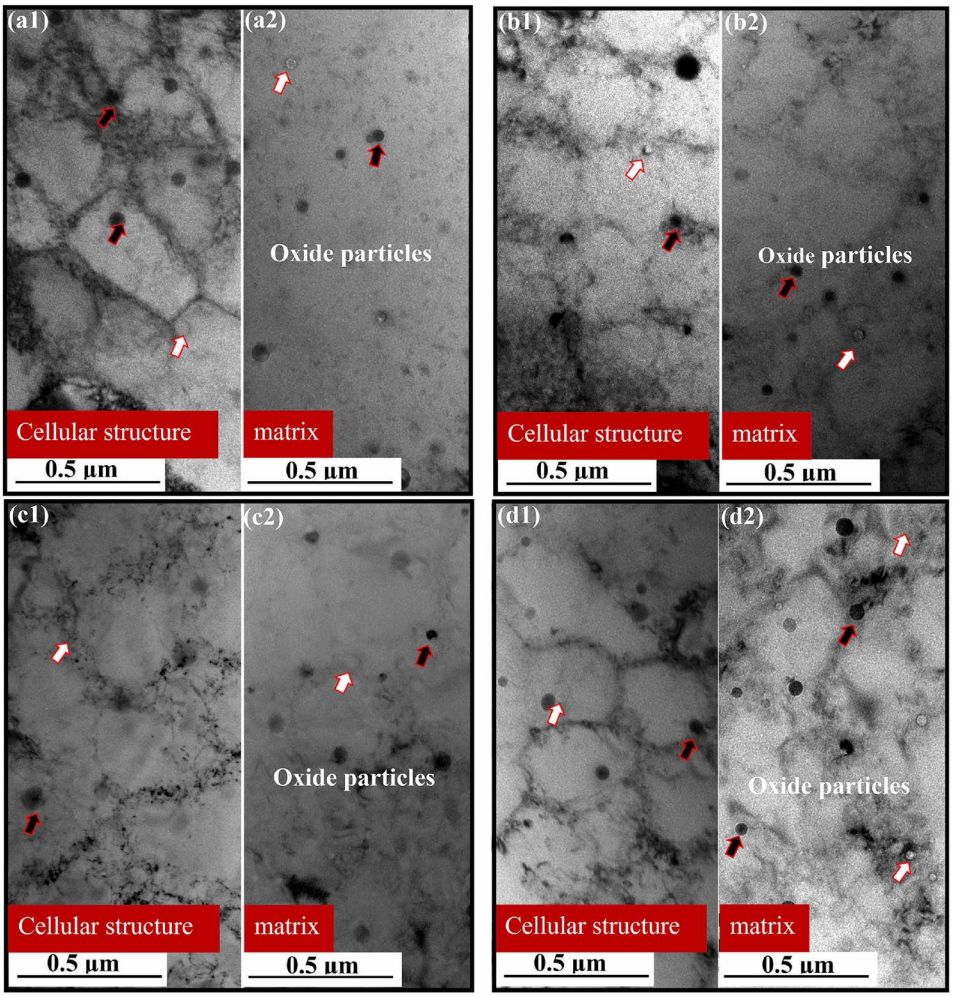

Fig. 5 (Color online) TEM images of oxide particles at cellular and noncellular structures: (a) 50 ppm, (b) 500 ppm, (c) 1000 ppm, and (d) 1500 ppm

termed the black particles. A significant positive correlation exists between the particle count and oxygen content. Figure 5a2–d2 shows the distributions of the nano-oxide particles in the noncellular areas of the LPBF 304 L SS substrate. Although the particle count increases with the oxygen content, for a given oxygen content level, there is no significant variation between the particle distributions in the cellular and noncellular structures. To delve deeper into the particle distributions across different oxygen contents, 13 TEM images were captured and statistically analyzed for each oxygen content level. The analysis results show that there is a substantial increase in the quantity of nano-oxide particles from 5.63522 particles/μm^2 at 50 ppm to 11.41485 particles/μm^2 at 1500 ppm.

To further elucidate the influence of the oxygen content on the nano-oxide particle composition, multiscale surface scanning analyses were performed on representative samples with the oxygen concentrations of 50 ppm and 1500 ppm. As shown in Fig. 6a–b, regardless of the oxygen concentration, the nano-oxide particles are primarily identified as Si-Cr-O and randomly dispersed across the cellular structure boundaries and interiors. Intriguingly, increasing the oxygen content led to the emergence of Mo-rich particles. This observation is consistent with those of Deng [14], who found that silicon was the principal chemical constituent of the oxides along with varying concentrations of other elements such as Mn and Cr. It is known that the high diffusion rate and strong affinity of Si for oxygen result in more Si oxides being produced in steel [32].

To investigate the reasons for the generation of the black and white nano-oxide particles in Fig. 5, high-magnification TEM characterization and EDS analyses were performed and the results are presented in Fig. 6. In Fig. 6a, the white nano-oxide particles are distinguished from the black ones based on the contrast in the 50 ppm samples. The EDS results for the 1500 ppm sample in Fig. 7 indicate that the primary components of both particle types are Si and O. The white particles contain more Si (21.1 wt. %) and O (35 wt.%) than the black particles (Si 7.0 wt.% and O 9.5 wt.%). The EDS results indicate extremely low contents of Si and O at the matrix region (a3) in contrast to the a1 and a2 particles, which are enriched with Si and O. Additionally, the black particles exhibit higher levels of Cr (15.7 wt. %) and Mo (2.3 wt.%) compared to the white oxide particles. This suggests that as the oxygen content increased, the oxide particles became enriched in Cr and Mo. The nano-oxide particles enriched in Cr and Mo formed under high-oxygen content conditions have irregular shapes.

Structural and chemical composition analyses were conducted on a specific particle (Fig. 8a) using TEM. The high-resolution TEM image in Fig. 8b shows its atomic arrangement while the corresponding diffraction pattern is shown in Fig. 8c. The elemental concentration of the particle was determined using EDX. The presence of such Mo-rich particles can improve the corrosion resistance of the material [22–24].

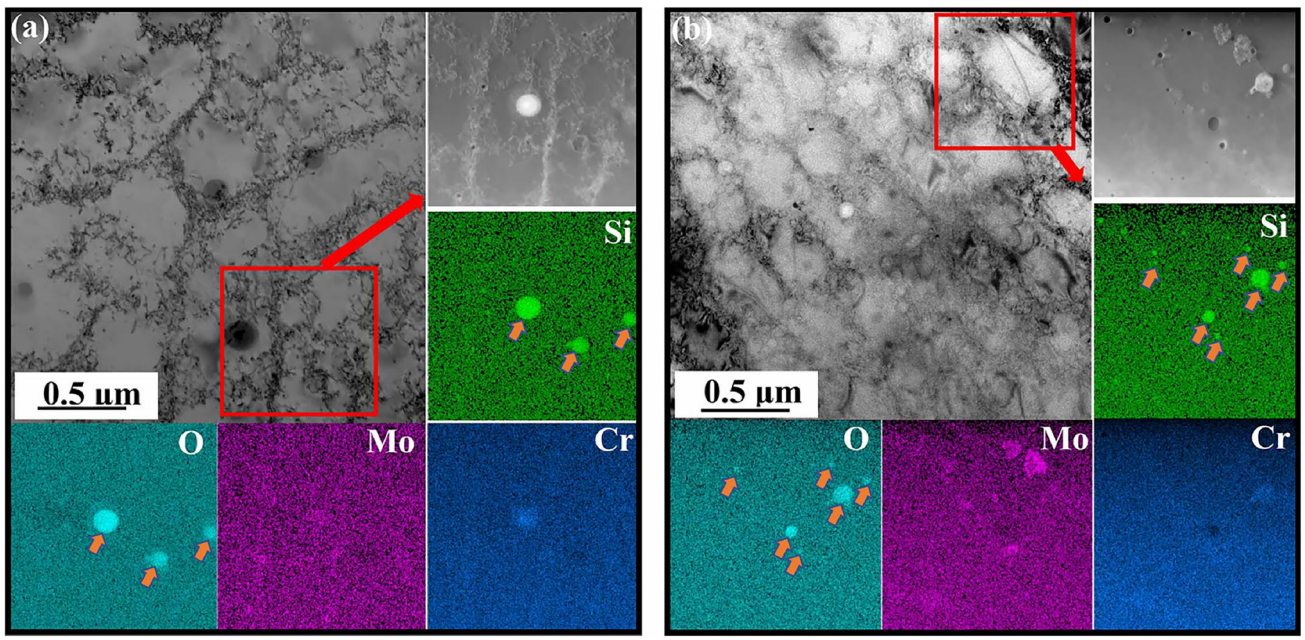

Fig. 6 (Color online) EDS mappings showing nano-oxide particle distributions: (a) 50 ppm, (b) 1500 ppm

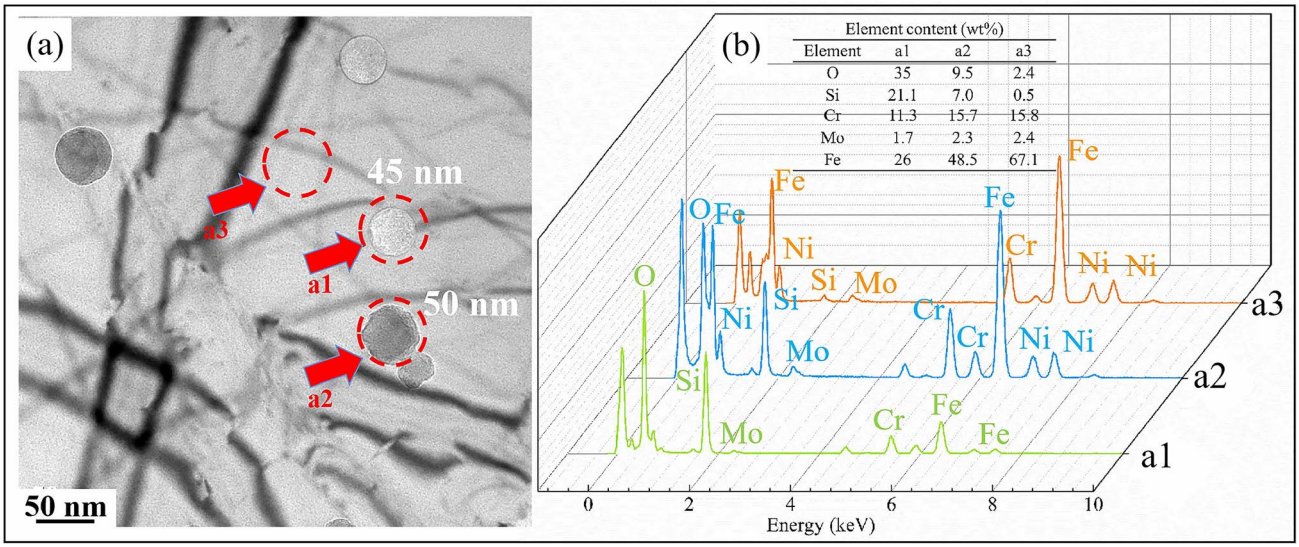

Fig. 7 (Color online) TEM image and EDS data of black and white nano-oxide particle and matrix samples (1500 ppm)

3.2 Mechanical properties

Figure 9a shows the engineering stress–strain curves for the samples with the four different oxygen concentrations. The quantitative UTS and YS results compiled in Table 2 indicate that the number of oxide particles and mechanical properties of the materials are affected by the wide-ranging variations in oxygen content.

The oxide particle density at 1500 ppm is approximately twice that at 50 ppm, which agrees well with the significantly increased strength of the former. The tensile test results indicate that increasing the oxygen content from 50 ppm to 1500 ppm led to a notable increase of 70 MPa in the YS (from 607.9 ± 38.5 MPa to 674.8 ± 23.08 MPa) whereas the effect on the UTS is relatively modest. Compared to previous studies, the YS is increased by at least 200 MPa compared to that of LPBF 304 L (485.2 ± 0.2 MPa) [15] and surpasses those of LPBF 304 L doped with 0.5 wt% yttrium oxide (575 ± 8 MPa) [18] and LPBF 316 L SS containing nano-sized SiO_2 oxide particles (548.35 MPa) [33]. In accordance with the Orowan strengthening mechanism, the ability of small dispersed nano-oxide particles to pin dislocations conferred enhanced strength at room temperature [34]. In addition, the abundance of ultrafine cellular structures within the grains further enhanced the mechanical properties of the material.

There is always a trade-off between the strength and ductility of a material. This study is no exception. The average EL of the samples shows a slight downward trend with increasing oxygen content. The EL is reduced by approximately 6% across samples with oxygen contents from 50 ppm(~ 46.6 ± 4.7%) to 1500 ppm(39.1 ± 1.6%). Despite this variation, the minimum EL is still 39.1%, which exceeds those of LPBF alloys doped with 0.5 wt.% yttrium oxide particles (approximately 32%) [18] and conventional ODS alloys (approximately 20.5%) [35]. The calculated YS-to-TS ratios of the samples are shown in Table 2. The ratio shows an upward trend and approaches 1 with increasing oxygen content. A higher YS-UTS ratio indicates that the material does not undergo plastic deformation under stress easily and has superior tensile properties and strength.

The tensile test results of the LPBF 304 L SS samples in this study are compared with those of other 304 L SS samples fabricated using AM and traditional methods with or without ODS in Fig. 9b. Across a wide range of oxygen contents, in situ LPBF-ODS 304 L SS has excellent yield strength and high elongation surpassing those of most ODS 304 L SS produced using LPBF and traditional manufacturing processes with Y_2O_3 particles added to the raw materials. This confirms that in situ alloying through oxygen regulation combined with AM is promising and feasible for manufacturing high-performance materials.

SEM analysis was performed on the tensile fracture surfaces of LPBF 304 L SS specimens with different oxygen contents (Fig. 10) to evaluate their fracture mechanisms in depth. Irrespective of the oxygen content, the macroscopic fracture surfaces (Fig. 10a–d) are identified as ductile fractures with notable dimples and necking phenomena. Detailed observations of specific regions (Fig. 10a1–a2) reveal the presence of numerous submicron-sized dimples with an approximate diameter of 250 nm. The fracture morphology reflects the favorable outcomes of significant plastic deformation prior to fracture. Delving deeper into the small dimples (Fig. 10(a2-d2)), nano-oxide particles are observed,

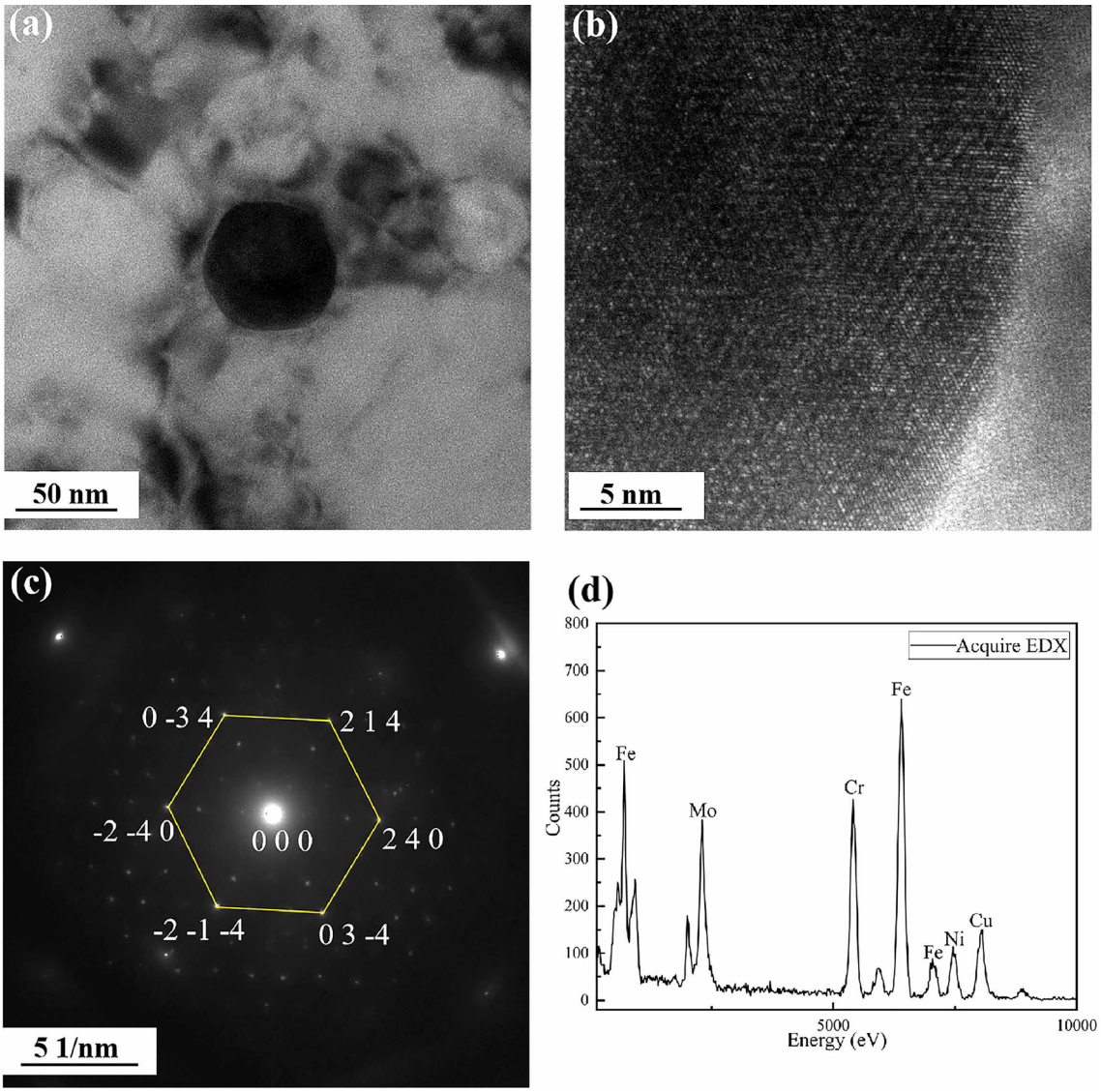

Fig. 8 (Color online) Calibration of σ phase: (a) transmission image morphology of σ phase, (b) microscopic morphology of σ phase at high magnification, (c) diffraction spot calibration of characterized spot, (d) EDS data of σ phase

some of which have diameters as large as 200 nm. These findings suggest that the larger particles may serve as potential crack initiation sites and eventually lead to material failure. Such insights into the microstructural aspects of fracture surfaces provide a more nuanced understanding of material behavior under stress.

3.3 Theoretical yield strength simulation

The tensile test results demonstrate a clear relationship between elevated oxygen contents and increased YS in LPBF-ODS 304 L SS. To provide a theoretical underpinning for these empirical findings, the theoretical YS values of the alloys with 50 ppm and 1500 ppm oxygen contents were calculated using Mechanical APDL2022R1. This comprehensive theoretical analysis allows for a more nuanced understanding of the influence of dispersed nano-oxide particles on the YS and EL of the material under both high and low oxygen content conditions.

The yield failure of the material was modeled in APDL using the von Mises criterion. This criterion, which is based on plasticity theory, is aligned with the fourth strength theory, which is also known as the distortion energy theory. It effectively describes the yield and failure behavior of a material under a three-dimensional stress state. Under this criterion, the material begins to yield once its per unit volume elastic potential energy (or elastic strain energy) crosses a specified threshold during deformation. Specifically, the von Mises criterion can be expressed as [36]

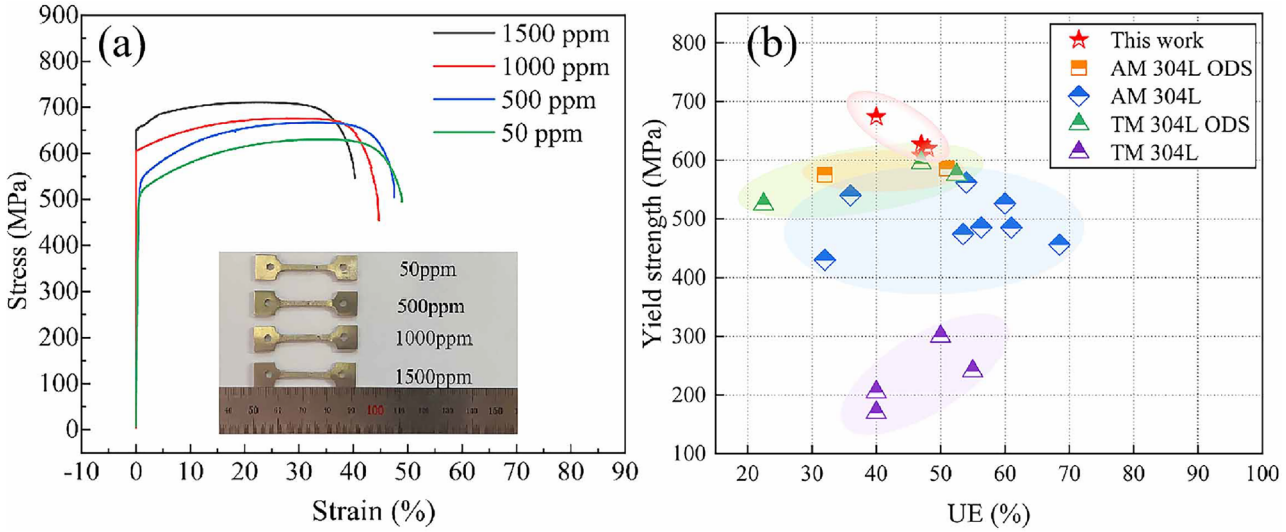

Fig. 9 (Color online) Mechanical properties of materials: (a) stress–strain curves from 50 ppm to 1500 ppm, (b) mechanical properties comparison [8, 15, 16, 31]

Table 2 Oxide particle number density and mechanical properties

Oxygen content (ppm)	Number density (particles/μm^2)	Yield strength (MPa)	Ultimate tensile strength (MPa)	Elongation (%)	Yield ratio (YS/UTS)
50	5.64	607.9 ± 38.5	696.7 ± 37.4	46.6 ± 4.7	0.87
500	5.65	619.1 ± 25.5	686.3 ± 47.1	47.4 ± 2.9	0.90
1000	9.55	626.8 ± 22.6	674.9 ± 28.3	46.6 ± 4.2	0.92
1500	11.41	674.8 ± 23.08	694.5 ± 20.3	39.1 ± 1.6	0.97

$$\left(\sigma_1-\sigma_2\right)^2+\left(\sigma_2-\sigma_3\right)^2+\left(\sigma_3-\sigma_1\right)^2=2\sigma_s^2=6K^2 \tag{1}$$

where σ_s is the yield point of the material and $K\left(T_S\right)$ its shear yield strength.

Material failure was assessed in APDL based on the fourth strength theory. This theory posits that material yield is caused by the shear energy density and assumes that the shape change energy density is the factor that causes material yield. This implies that irrespective of the stress condition of a component, plastic yield occurs at any point where the shape change energy density reaches the threshold value of the material [36], as observed during uniaxial tensile yield. This concept is encapsulated in the theoretical equation (2) for the shape change energy density within the material and equation (3) for the shape change energy density of the material under uniaxial tensile conditions. Equation (4) outlining the theoretical conditions for material failure was derived from these equations. Moreover, the random distributions of nano-oxide particles with varying oxygen contents were incorporated into the simulation. This addition allowed the corresponding theoretical strength values under different oxygen contents to be calculated and the impact of these particles on the elongation of the material to be assessed.

The shape change energy density at a point inside the material is given by [36]

$$U_d=(1+U)\frac{\left(\sigma_1-\sigma_2\right)^2+\left(\sigma_2-\sigma_3\right)^2+\left(\sigma_3-\sigma_1\right)^2}{6E}. \tag{2}$$

Under uniaxial tensile conditions where $\sigma_1=\sigma_S$ and $\sigma_2=\sigma_3=0$, the limiting value of the shape change specific energy at this point is

$$U_u=(1+U)\frac{\left(\sigma_s\right)^2}{3E}. \tag{3}$$

It follows that the condition for damage to occur in the material is

$$\begin{aligned}U_d&=(1+U)\frac{\left(\sigma_1-\sigma_2\right)^2+\left(\sigma_2-\sigma_3\right)^2+\left(\sigma_3-\sigma_1\right)^2}{6E}\\&\geq(1+U)\frac{\left(\sigma_s\right)^2}{3E}.\end{aligned} \tag{4}$$

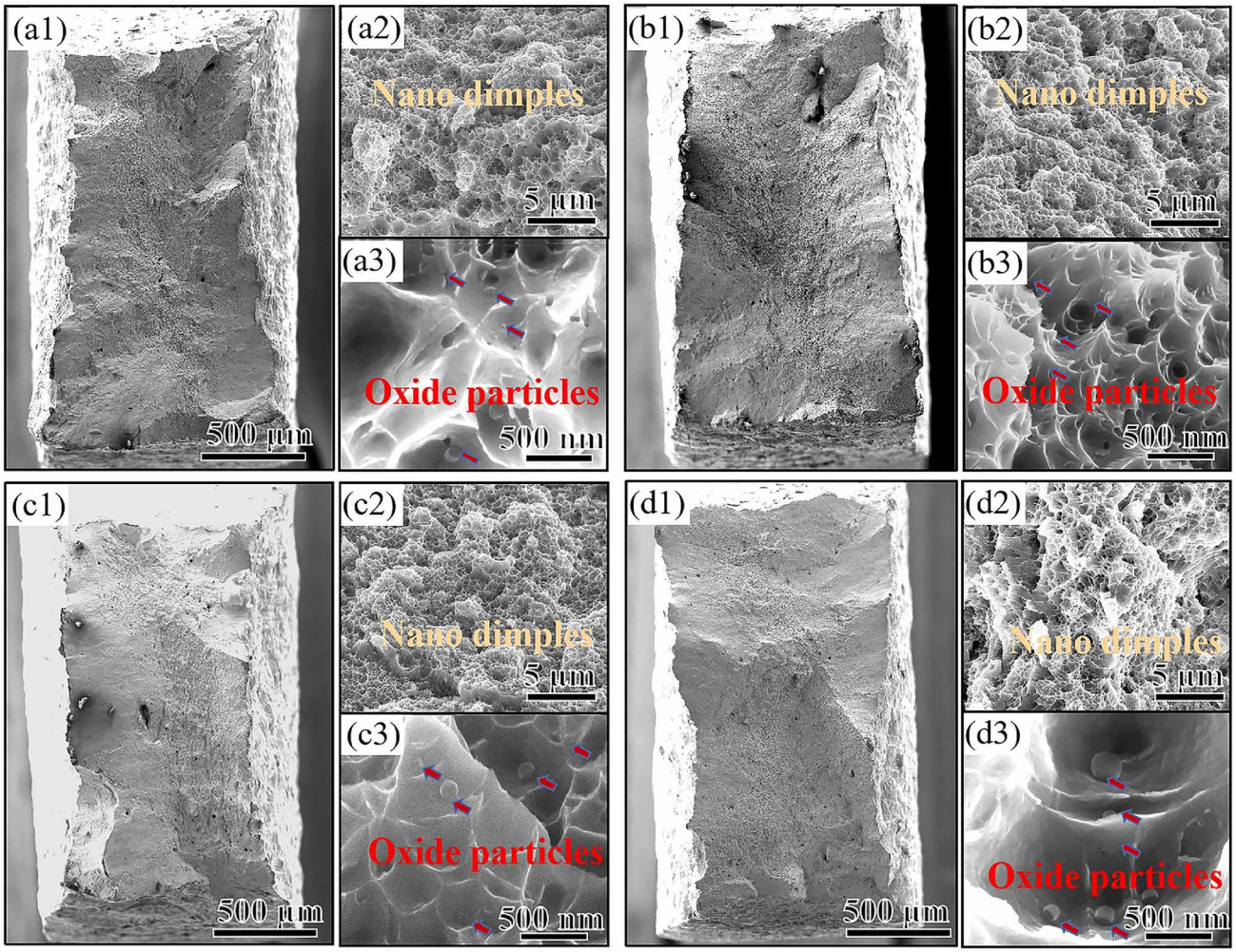

Fig. 10 (Color online) Fracture morphologies and oxide particle distributions at 50–1500 ppm oxygen levels: (a1-d1) macroscopic fracture morphologies, (a2-d2) nano-tough nests, (a3-d3) oxide particles at tough nests

Information on the number density and types of nano-oxide particles was obtained from the experimental TEM results. Two distinct oxygen content states comprising the 50 ppm and 1500 ppm states were configured in the simulation. The theoretical mechanical properties for each unit area $\left(1\ \mu m^2\right)$ of the material were calculated by simulating the room-temperature tensile process in a tensile testing machine. Table 2 presents the densities of nano-oxide particles per square micrometer across an oxygen content range of 50 ppm to 1500 ppm. In the idealized model, the particles were defined as SiO_2 (elastic modulus 700 GPa, Poisson's ratio 0.23) and the matrix material as 304 L SS (elastic modulus 210 GPa, Poisson's ratio 0.3). Considering that nano-oxide particles were randomly generated during the printing process and that the tensile process in the tensile testing machine occurred at room temperature, the simulation must incorporate not only the random distribution of nano-oxide particles but also realistic temperature and material constraint settings. The temperature was set to 25 °C with a fixed constraint applied to the left side whereas the right side was subjected to loading, as illustrated in Fig. 11a1 and Fig. 11b1. Several nonlinear parameters such as the large deformation option, prediction correction, and stress-stiffening function were adjusted during the simulation calculation process.

The mechanical properties of the material were simulated and the predicted YS at the oxygen contents of 50 ppm and 1500 ppm shown in Fig. 11a2 and Fig. 11b2), respectively. The predicted YS at 1500 ppm is 688 MPa. The increase in YS compared to the YS of 618 MPa at 50 ppm is attributed to the dispersed distribution of the nano-oxide particles, which also contributed to significant stress concentration. Considering the EL values of 46.6% at 50 ppm and 39.1% at 1500 ppm, an intermediate tensile elongation rate of 40% was used to assess the effect of the oxygen content on

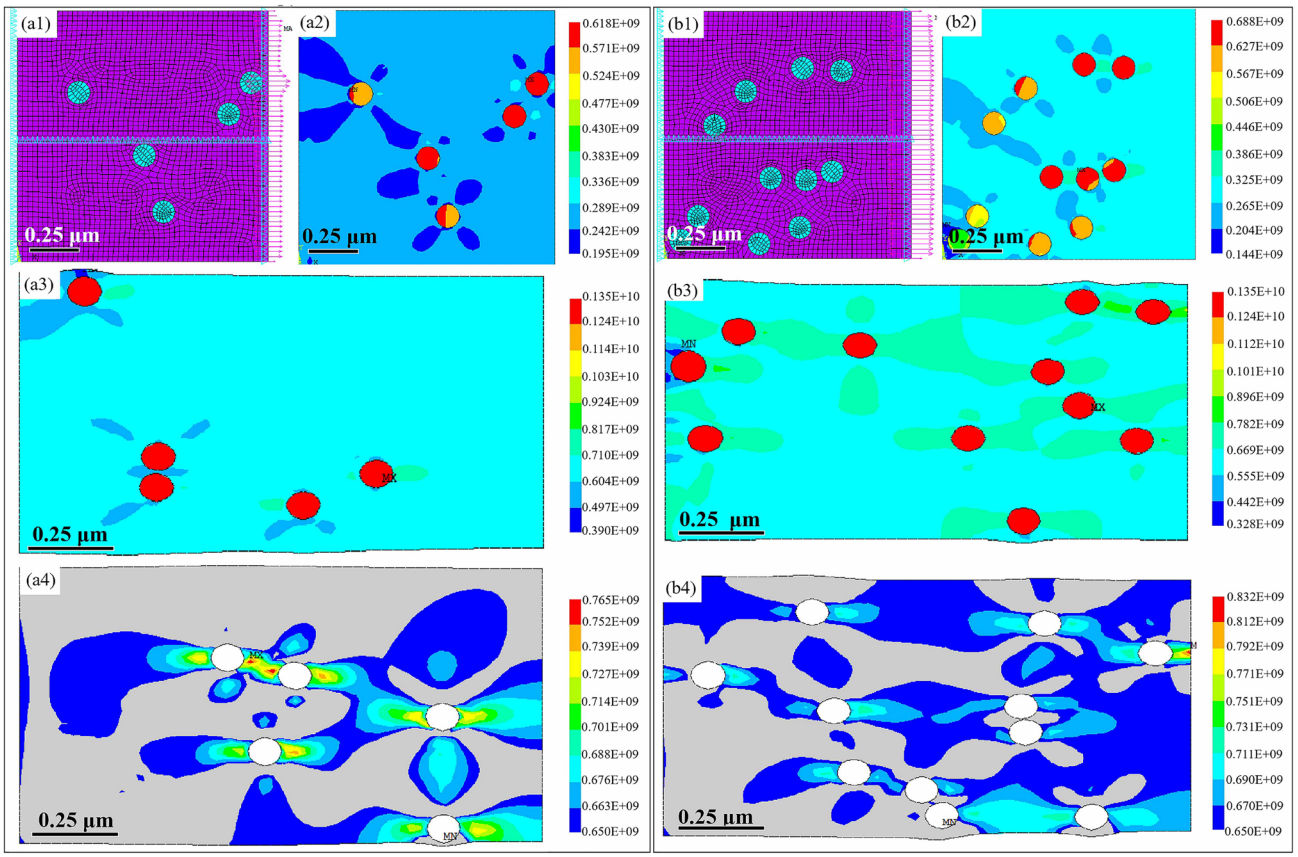

Fig. 11 (Color online) Simulation of theoretical YS at 50 ppm and 1500 ppm oxygen contents: a1–b1 schematic diagrams of fixed constraint and displacement deformation, a2–b2 theoretical YS values, (a3-b3) tensile strength of oxide particles, (a4-b4) tensile strength of substrate

material ductility. Comparing the tensile strengths of the nano-oxide particles (Fig. 11a3 and Fig. 11b3) and matrix (Fig. 11a4 and Fig. 11b4), it is evident that the nano-oxide particles are considerably harder and possess higher tensile strength than the matrix. Thus, the overall theoretical tensile fracture YS is predominantly determined by the fracture failure value of the matrix. Analysis of the fracture failure cloud map indicates that increasing the number of nano-oxide particles per unit area results in an enlarged failure zone for a given displacement during tensile testing. Consequently, the material tends to fail earlier, leading to reduced ductility.

4 Discussion

The oxygen content in the processing chamber can be controlled during the LPBF process for the in situ production of oxide particles. Hsu et al. [23] reported the preparation of ODS steel by increasing the oxygen content to 500 ppm during the LPBF process. In this study, a wider oxygen content range was explored for in situ LPBF-ODS material preparation to determine the fundamental mechanisms for enhancing material performance.

4.1 Strengthening mechanisms of in situ LPBF-ODS 304 L SS

The connection between the microstructure and mechanical properties (Fig. 9) of in situ LPBF-ODS 304 L SS is established in this section and the potential mechanisms for achieving high material performance through LPBF discussed. As the oxygen content increased, the YS was found to increase by approximately 149.9 ~ 216 MPa compared to that of LPBF 304 L SS without in situ oxygen synthesis alloying. This suggests that the presence of nano-oxide particles and a smaller cell size are advantageous for enhancing material strength. The oxygen content affects the temperature and cooling rate of the molten pool owing to its impact on the thermophysical properties of the metal, such as its thermal conductivity and specific heat capacity. The resultant changes in these properties due to the introduction of oxygen alter the manner in which heat is transferred and dissipated in the molten material, thereby influencing the cooling rate. Additionally, oxygen can change the surface energy of the melt, which affects the dynamics of the molten pool and the solidification patterns, leading to cellular structures. Moreover, interactions between the nano-oxide particles and

growing cells during the solidification stage can split the tips of the cells into smaller cells. The repeated interactions of the nano-oxide particles with one another lead to shape deformation. Further statistical analysis of the oxide particle size and quantity by integrating the TEM images reveals that the particle size remained stable (~ 46 nm) while the particle density increased with increasing oxygen content. This increase in oxide particle density corresponds to an increase in the YS and a slight decrease in the EL. Table 2 shows that the 1500 ppm sample has a high yield ratio (0.97), which is primarily attributed to the increased in situ formation of oxide particles within the sample under high-oxygen content conditions. These particles acted as pinning points that hindered dislocation motion and thereby increased the YS of the material [33]. However, an excessive quantity of hard particles can lead to local stress concentration and cause material failure, reduce elongation [18], and ultimately result in a high yield ratio. A higher YS/UTS ratio indicates that the material does not easily undergo plastic deformation under stress and has better tensile properties and strength.

The simulation results in Fig. 11a2 and b2 suggest that a high density of oxide particles is likely to cause more stress localization around the particles, which plays an important role in impeding dislocation movement. A higher particle density therefore strengthens the material effectively by introducing more obstacles to dislocation movement during deformation. However, the stress localization due to the nano-oxide particles is detrimental to material ductility because of the more severe deformation around these high-hardness particles. Once the localized deformation exceeds the ductility limit of the material, microcracks can form and coalesce between the hard particles and weak matrix, leading to premature failure. The simulation outcomes are consistent with the empirical observations and confirm that increasing the number of oxide particles enhances material strength but reduces ductility.

Figure 12 shows the random distribution of the nano-oxide particles and the mechanism for mechanical property enhancement at different oxygen contents during the LPBF process. The particles in the material impeded dislocation movement and led to dislocation pileups and tangles. The hindered movement of high-density dislocations caused material hardening and strengthening. This is the root cause of the enhanced YS at higher oxygen contents. Combining the oxide microstructural characteristics in Figs. 5 and 6, it is clear that nano-oxide particles were randomly dispersed throughout the matrix at the boundaries or inside the cell structures with a few smaller-sized particles in between them. Both the distribution and size of the particles affected dislocation movement through the dislocation shearing and bypass mechanisms. The bypass mechanism is applicable for larger particles. The dislocation loops or rings formed around the particles acted as obstacles within the lattice, which impeded dislocation movement and thereby increased the YS [8]. In contrast, the smaller particles facilitated the shearing mechanism by allowing dislocations to cut through the particles and continue to move within the lattice. In this case, the material strength was enhanced without sacrificing the ductility excessively. This is why the YS was increased by 70 MPa while the EL remained at 39% in the samples with 1500 ppm oxygen content.

Differences in oxygen content can also lead to compositional diversity in the oxide particles. Fig. 13(a) shows the Gibbs free energies of several oxides. The standard Gibbs free energy change of SiO_2 is lower than those of Cr, Mo, Fe, and Mn oxides at all temperatures [37]. Figure 13(b) and Fig. 13(c) shows that SiO_2 has a lower constant-pressure heat capacity of 35 J/(mol K) and total enthalpy of (−400 kJ/mol), which suggests that SiO_2 can form stably in spontaneous exothermic reactions. In addition, previous studies [37] have shown that the equilibrium partial pressure of Si at 1673 K is approximately 2.4×10^{-20} atm. This implies that Si can be preferentially and stably oxidized to provide oxygen partial pressures greater than 2.4×10^{-20} atm. This conclusion is consistent with our observation that the dominant oxide particles are SiO_2 with a few particles enriched with Cr/Mo under low- and high-oxygen conditions. This can be attributed to the high content of Cr and small amounts of Si in the samples, in which the excess oxygen reacted not only with Si but also with Cr and Mo in the metal matrix.

4.2 Theoretical strength contributions

It has been widely reported that excellent strength and good ductility can be obtained in LPBF SS owing to ultrafine cellular subgrains with dimensions of approximately 500 nm [15, 31, 38]. The cellular subgrains in this study, which are approximately 330 nm in size, are finer than those in previously published results. The enhanced material strength in this study is primarily attributed to the finer cellular structure compared with those of previous LPBF 304 L and ODS alloys. Another important factor is the augmented number of oxide particles. The oxide particles impact dislocation strengthening by both pinning dislocations inside the cells and acting as impediments to dislocation movement during tensile deformation. To elucidate the specific contributions of the dislocation density and the presence of oxide particles to material strength, the theoretical increase in YS $(\Delta\sigma_y)$ is estimated as

$$\Delta\sigma_y = \Delta\sigma_D + \Delta\sigma_{or} \tag{5}$$

where $\Delta\sigma_y$ is the YS increment, $\Delta\sigma_D$ the dislocation strengthening contribution, and $\Delta\sigma_{or}$ the oxide particle strengthening contribution.

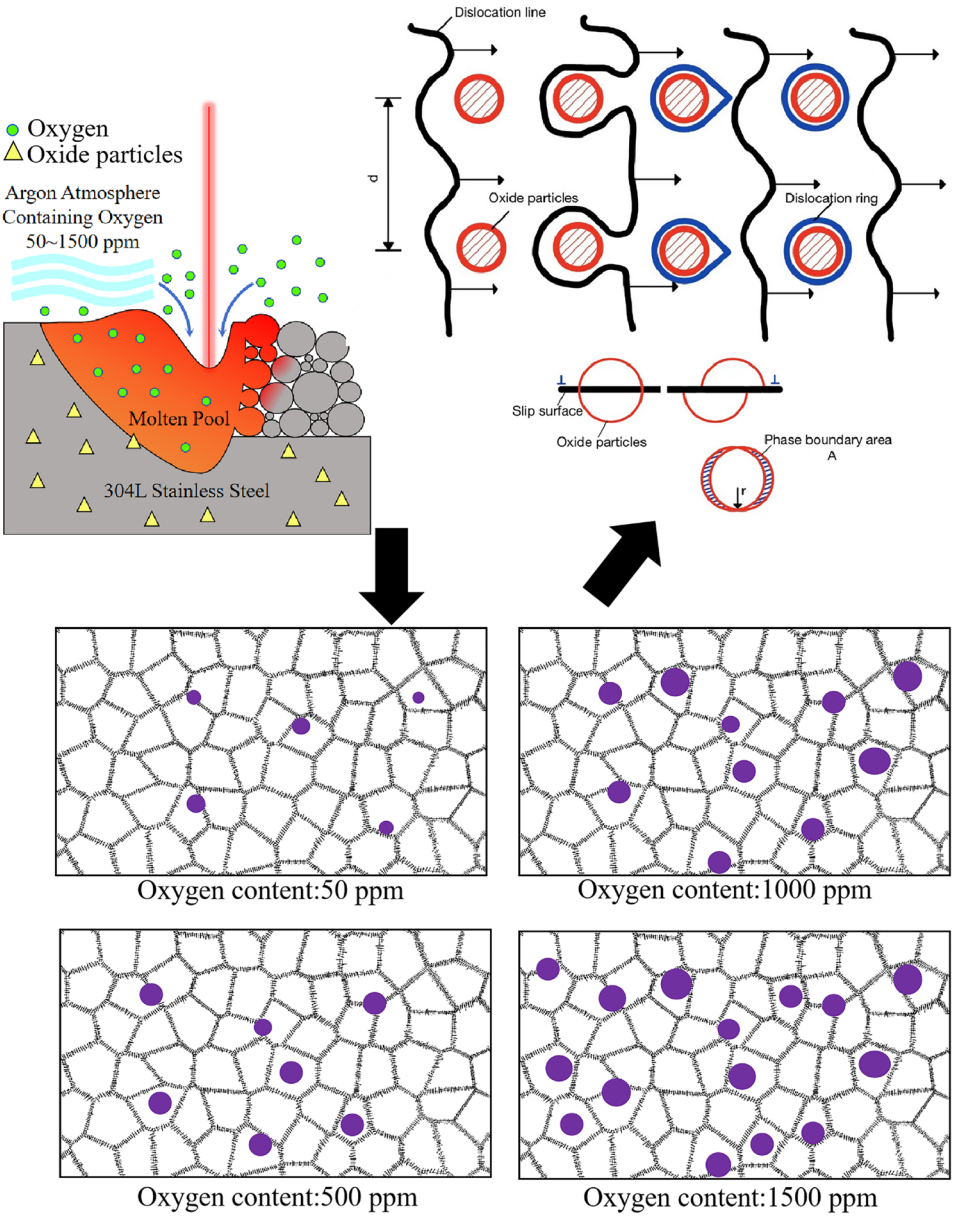

Fig. 12 (Color online) Oxide particle formation mechanism

It is generally accepted that the GND density is proportional to the average KAM [39, 40]. The average value of KAM(0.4 − 0.5) under different oxygen contents in this study is higher than the average KAM of approximately 0.310 in LPBF 304 L SS without in situ oxygen synthesis. Following the theory proposed by Gao and Kubin [40], the dislocation GND density (ρ) can be characterized through the KAM and calculated as

$$\rho_{GND} = \frac{2KAM_{\mathrm{av}}}{\mu b} \tag{6}$$

where KAM_{av} is the average KAM value, μ the step size (0.6 μm), and b the Burgers vector (0.25 nm). The dislocation density can be considered to be linearly related to the GND density [39]. As a rough estimate, the total dislocation density was assumed to be 1.5 times the GND density [40]. The estimated total dislocation densities in this study and in previous studies are hence 41×10^{14} m^{-2}(50 ppm) and 56×10^{14} m^{-2}(1500 ppm), respectively.

These results indicate that the dislocation density increases with the oxygen content. The contribution of dislocation strengthening is commonly estimated using the Bailey–Hirsch equation [41]

$$\Delta\sigma_D = \alpha MGb\left(\rho_{ODS}^{0.5} - \rho_M^{0.5}\right) \tag{7}$$

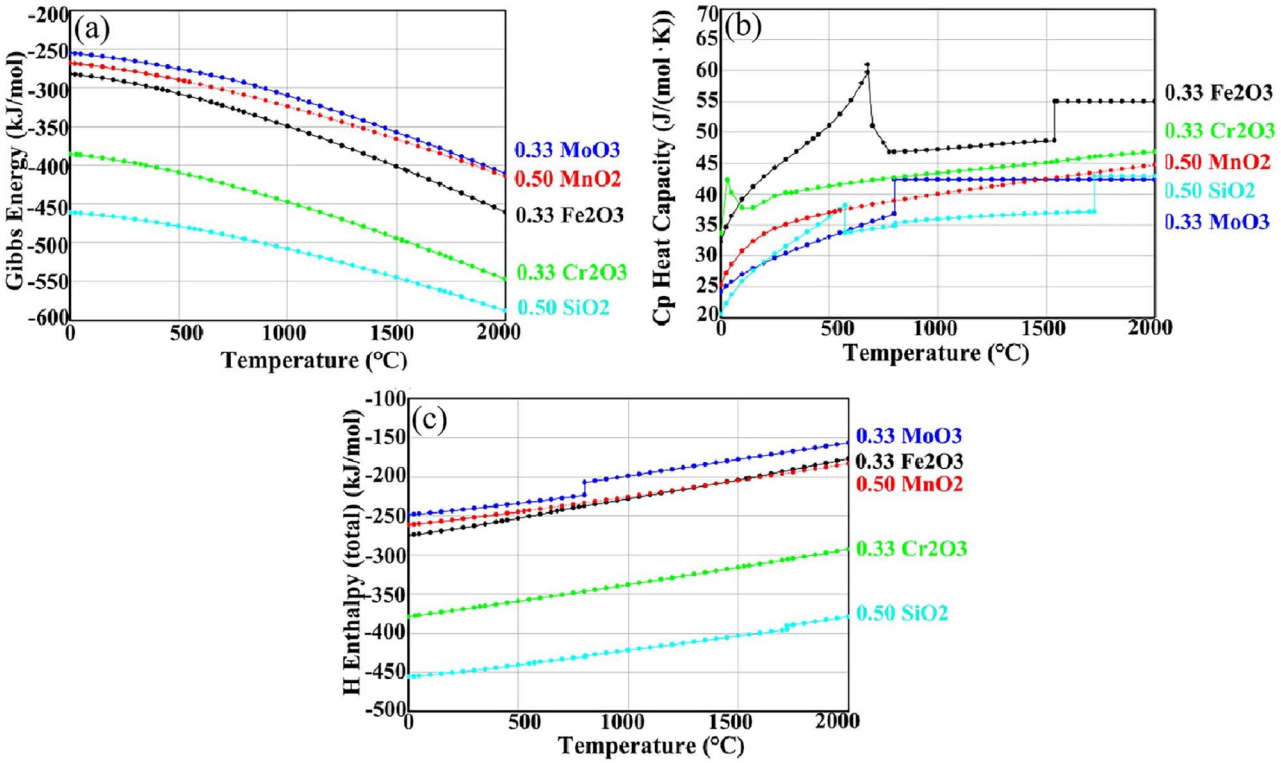

Fig. 13 (Color online) Thermodynamic calculations and simulations of different oxide particles: (a) Gibbs free energies, (b) constant-pressure heat capacities, (c) total enthalpies of oxides

where α is a constant (0.25), M the Taylor factor (usually taken as 3 for fcc polycrystals), G the shear modulus (78 GPa), b the Burgers vector (0.25 nm), and ρ the dislocation density $\left(\mathrm{m}^{-2}\right)$ [18, 42]. The calculated dislocation strengthening contribution to the YS $\left(\Delta\sigma_D\right)$ is approximately 219.375 MPa. Numerous studies have highlighted the effects of nano-sized particles within the matrix on mechanical performance by impeding dislocation movement [40]. The randomly distributed oxide particles at the grain boundaries or interior grains reinforce the material by impeding and stacking dislocations.

By adjusting the oxygen concentration during the LPBF process, the number of oxide particles could be adjusted from 0.624 vol% to 1.264 vol% with an average size of approximately 46 nm. The contribution of oxide particles to material reinforcement can be evaluated through the Orowan strengthening due to dislocation–particle interaction [43]:

$$\Delta\sigma_{\mathrm{or}} = \left(\frac{0.84MGbf_v^{1/2}}{2\pi(1-v)^{1/2}r\left(\frac{2\pi}{3}\right)^{1/2}}\right)\ln\left(\frac{r}{b}\right) \tag{8}$$

where $\Delta\sigma_{\mathrm{or}}$ is the precipitation strengthening increment, f the volume fraction of the precipitation (vol%), and D the average particle diameter (μm). Here, D was measured to be 46 nm, and the f values are 0.624 vol% and 1.265 vol% at 50 ppm and 15 ppm, respectively. The calculation results reveal strength increments of 23 MPa to 152 MPa for oxygen contents from 50 ppm to 1500 ppm. This suggests that increasing the number of nano-oxide particles contributes to material reinforcement favorably.

Based on the above calculations, it is evident that the formation of finer cellular structures and high-density dispersed oxide particles significantly reinforce in situ LPBF-ODS 304 L SS. The higher oxygen content is pivotal in the increased material strength compared to that of LPBF 304 L without in situ oxygen synthesis with a maximum increase of 219.375 MPa in YS at 1500 ppm oxygen content. The direct contribution of the oxide particles to material strengthening is approximately 152 MPa at 1500 ppm, which is significantly higher than the 129 MPa contribution at 50 ppm. These findings provide a prospective approach for developing complex structural components suitable for the harsh service environments in nuclear power plants.

5 Conclusion

The microstructure and mechanical performance of in situ LPBF-ODS 304 L SS were investigated in detail in this study through a series of oxygen content controls with the aim of improving our understanding of the relationship between oxide dispersion and the mechanical performance of LPBF-ODS 304 L SS. The main conclusions are as follows:

(1) The in situ LPBF-ODS 304 L SS samples have a finer cellular subgrain structure of approximately ~ 330 nm size, which is notably smaller than the ~ 500 nm cellular structure observed in LPBF 304 L SS.
(2) The in situ LPBF-ODS 304 L SS samples have high yield strength and maintain comparatively good ductility surpassing those of both LPBF 304 L and most conventionally manufactured austenitic ODS alloys. The increased YS of the LPBF 304 L ODS alloy is mainly attributed to dispersed nanoparticles $\left(SiO_2 \text{ and } Si-Cr-O\right)$.
(3) The simulation results for the mechanical properties indicate that an increased concentration of oxide particles is correlated with a rise in the theoretical YS of the material. The higher concentration of particles also leads to additional stress concentration, which results in a reduction in the EL of the material.

Author Contributions All authors contributed to the study conception and design. Material preparation, data collection, and analysis were performed by Yan-Lin Gu, Juan Hou, and Fan Yang. The first draft of the manuscript was written by Yan-Lin Gu, and all authors commented on previous versions of the manuscript. All authors read and approved the final manuscript.

Data availability The data that support the findings of this study are openly available in Science Data Bank at https://cstr.cn/31253.11.sciencedb.13199 and https://doi.org/10.57760/sciencedb.13199 .

Declarations

Conflict of interest The authors declare that they have no Conflict of interest.

References

1. K.L. Murty, I. Charit, Structural materials for Gen-IV nuclear reactors: Challenges and opportunities. J. Nucl. Mater. **383**, 189–192 (2008). https://doi.org/10.1016/j.jnucmat.2008.08.044
2. N. Oono, S. Ukai, S. Kondo et al., Irradiation effects in oxide dispersion strengthened (ODS) Ni-base alloys for Gen. IV nuclear reactors. J. Nucl. Mater. **465**, 835–842 (2015). https://doi.org/10.1016/j.jnucmat.2015.06.057
3. L. Zhang, X.W. Chen, Y. Dai et al., Design and analysis of a heat-pipe molten salt reactor tower thermal power generation system. Nucl. Tech. (in Chinese) **46**, 070601 (2023). https://doi.org/10.11889/j.0253-3219.2023.hjs.46.070601
4. L.H. He, J.M. Li, H.W. Zhang et al., Effect of heat treatment on the microstructure and mechanical property of GX4CrNi13-4 manufactured by laser cladding. Nucl. Tech. (in Chinese) **47**, 060503 (2024). https://doi.org/10.11889/j.0253-3219.2024.hjs.47.060503
5. H. Liu, S.L. Min, M.L. Jiang et al., Helium bubble growth in He^+ ions implanted 304L stainless steel processed by laser powder bed fusion during post-irradiation annealing at 600 °C. Acta. Metall. Sin-Engl. **35**, 1509–1520 (2022). https://doi.org/10.1007/s40195-022-01391-w
6. X.P. Li, C.W. Kang, H. Huang et al., Selective laser melting of an $Al_{86}Ni_6Y_{4.5}Co_2La_{1.5}$ metallic glass: Processing, microstructure evolution and mechanical properties. Mat. Sci. Eng. A-Struct. **606**, 370–380 (2014). https://doi.org/10.1016/j.msea.2014.03.097
7. M. Ghayoor, S.B. Badwe, H. Irrinki et al., Water atomized 17–4 PH stainless steel powder as a cheaper alternative powder feedstock for selective laser melting. Mater. Sci. Forum **941**, 698–703 (2018). https://doi.org/10.4028/www.scientific.net/MSF.941.698
8. M.B. Wilms, S.K. Rittinghaus, M. Gossling et al., Additive manufacturing of oxide-dispersion strengthened alloys: materials, synthesis and manufacturing. Prog. Mater Sci. **133**, 101049 (2023). https://doi.org/10.1016/j.pmatsci.2022.101049
9. P.K. Kumar, N.V. Sai, A.G. Krishna et al., Fabrication and microstructural evaluation of ODS austenitic stainless steels through mechanical alloying. Mater. Today-Proc. **23**, 465–470 (2020). https://doi.org/10.1016/j.matpr.2019.04.207
10. Y. Zhong, L.F. Liu, J. Zou et al., Oxide dispersion strengthened stainless steel 316L with superior strength and ductility by selective laser melting. J. Mater. Sci. Technol. **42**, 97–106 (2020). https://doi.org/10.1016/j.jmst.2019.11.004
11. W. Zhai, W. Zhou, S. Nai et al., Characterization of nanoparticle mixed 316 L powder for additive manufacturing. J. Mater. Sci. Technol. **47**, 162–170 (2020). https://doi.org/10.1016/j.jmst.2020.02.019
12. J.T. Sehrt, S. Kleszczynski, C. Notthoff, Nanoparticle improved metal materials for additive manufacturing. Progress in Additive Manufacturing. **2**, 179–186 (2017). https://doi.org/10.1007/s40964-017-0028-9
13. Y.L. Xu, Z.J. Zhou, M. Li et al., Fabrication and characterization of ODS austenitic steels. J. Nucl. Mater. **417**, 283 (2011). https://doi.org/10.1016/j.jnucmat.2010.12.155
14. P. Deng, M. Song, J. Yang et al., On the thermal coarsening and transformation of nanoscale oxide inclusions in 316L stainless steel manufactured by laser powder bed fusion and its influence on impact toughness. Mat. Sci. Eng. a-Struct. **835**, 142690 (2022). https://doi.org/10.1016/j.msea.2022.142690
15. J. Hou, W. Chen, Z. Chen et al., Microstructure, tensile properties and mechanical anisotropy of selective laser melted 304L stainless steel. J. Mater. Sci. Technol. **48**, 63 (2020). https://doi.org/10.1016/j.jmst.2020.01.011
16. M. Ghayoor, K. Lee, Y.J. He et al., Selective laser melting of 304L stainless steel: Role of volumetric energy density on the microstructure, texture and mechanical properties. Addit. Manuf. **32**, 101011 (2020). https://doi.org/10.1016/j.addma.2019.101011
17. B. AlMangour, D. Grzesiak, J.M. Yang, Rapid fabrication of bulk-form TiB2/316L stainless steel nanocomposites with novel reinforcement architecture and improved performance by selective laser melting. J. Alloy. Compd. **680**, 480 (2016). https://doi.org/10.1016/j.jallcom.2016.04.156
18. M. Ghayoor, K. Lee, Y.J. He et al., Selective laser melting of austenitic oxide dispersion strengthened steel: Processing, microstructural evolution and strengthening mechanisms. Mat. Sci. Eng. a-Struct. **788**, 139532 (2020). https://doi.org/10.1016/j.msea.2020.139532

19. Q.L. Guo, C. Zhao, M.L. Qu et al., In-situ full-field mapping of melt flow dynamics in laser metal additive manufacturing. Addit. Manuf. **31**, 100939 (2020). https://doi.org/10.1016/j.addma.2019.100939
20. L. Wang, S. Burns, D.E. Giammar et al., Element mobilization from Bakken shales as a function of water chemistry. Chemosphere **147**, 286–293 (2016). https://doi.org/10.1016/j.chemosphere.2016.01.107
21. T.M. Smith, C.A. Kantzos, N.A. Zarkevich et al., A 3D printable alloy designed for extreme environments. Nature **617**, 513 (2023). https://doi.org/10.1038/s41586-023-05893-0
22. J.U. Rakhmonov, C. Kenel, A. De Luca et al., Effect of Y2O3 dispersoids on microstructure and creep properties of Hastelloy X processed by laser powder-bed fusion. Addit. Manuf. Lett. **3**, 100069 (2022). https://doi.org/10.1016/j.addlet.2022.100069
23. T.H. Hsu, Y.J. Chang, C.Y. Huang et al., Microstructure and property of a selective laser melting process induced oxide dispersion strengthened 17–4 PH stainless steel. J. Alloy. Compd. **803**, 30 (2019). https://doi.org/10.1016/j.jallcom.2019.06.289
24. M.H. Song, X. Lin, F.G. Liu et al., Effect of environmental oxygen content on the oxide inclusion in laser solid formed AISI 420 stainless steel. Mater. Design **90**, 459 (2016). https://doi.org/10.1016/j.matdes.2015.11.003
25. W.S. Shin, B. Son, W.S. Song et al., Heat treatment effect on the microstructure, mechanical properties, and wear behaviors of stainless steel 316L prepared via selective laser melting. Mat. Sci. Eng. a-Struct. **806**, 140805 (2021). https://doi.org/10.1016/j.msea.2021.140805
26. E. Liverani, S. Toschi, L. Ceschini et al., Effect of selective laser melting (SLM) process parameters on microstructure and mechanical properties of 316L austenitic stainless steel. J. Mater. Process. Tech. **249**, 255 (2017). https://doi.org/10.1016/j.jmatprotec.2017.05.042
27. R.D. Li, Y.S. Shi, Z.G. Wang et al., Densification behavior of gas and water atomized 316L stainless steel powder during selective laser melting. Appl. Surf. Sci. **256**, 4350 (2010). https://doi.org/10.1016/j.apsusc.2010.02.030
28. B.C. Zhang, L. Dembinski, C. Coddet, The study of the laser parameters and environment variables effect on mechanical properties of high compact parts elaborated by selective laser melting 316L powder. Mat. Sci. Eng. A-Struct. **584**, 21 (2013). https://doi.org/10.1016/j.msea.2013.06.055
29. P. Saxena, H. Gajera, D.R. Shah et al., Effect of SLM process parameters on hardness and microstructure of stainless steel 316 material. Mater. Today-Proc. **50**, 1653 (2022). https://doi.org/10.1016/j.matpr.2021.09.144
30. L.M. Li, S.Y. Jiang, Z.P. Chen et al., Mesh-based activation analysis for structural materials in nuclear reactor. Nucl. Tech. (in Chinese) **45**, 080601 (2022). https://doi.org/10.11889/j.0253-3219.2022.hjs.45.080601
31. F. Yang, D. Zhu, M. Jiang et al., Effect of heat treatment on the microstructure, mechanical properties and corrosion resistance of selective laser melted 304L stainless steel. Acta. Metall. Sin-Engl. **35**, 1688 (2022). https://doi.org/10.1007/s40195-022-01430-6
32. H. Yin, B. Wei, A. Shmatok et al., On the nanoscale oxide dispersion via in-situ atmospheric oxidation during laser powder bed fusion. J. Mater. Process. Tech. **322**, 118191 (2023). https://doi.org/10.1016/j.jmatprotec.2023.118191
33. Y. Chen, X. Wang, D. Li et al., Experimental characterization and strengthening mechanism of process-structure-property of selective laser melted 316 L. Mater. Charact. **198**, 112753 (2023). https://doi.org/10.1016/j.matchar.2023.112753
34. Q.S. Song, Y. Zhang, Y.F. Wei et al., Microstructure and mechanical performance of ODS superalloys manufactured by selective laser melting. Opt. Laser Technol. **144**, 107423 (2021). https://doi.org/10.1016/j.optlastec.2021.107423
35. W.Z. Shi, L.M. Yu, C.X. Liu et al., Evolution of Y2O3 precipitates in ODS-316 L steel during reactive-inspired ball-milling and spark plasma sintering processes. Powder Technol. **398**, 117072 (2022). https://doi.org/10.1016/j.powtec.2021.117072
36. ANSYS Mechanical APDL Theory Reference. Theory statistics retrieved from https://www.ansys.com/dam/jcr:c24843b9-2c8e-43b3-9d89-74a3b2e2a3db/ansys-mechanical-apdl-theory-reference, (2021)
37. K. Saeidi, L. Kvetkova, F. Lofajc et al., Austenitic stainless steel strengthened by the in situ formation of oxide nanoinclusions. RSC Adv. **5**, 20747–20754 (2015). https://doi.org/10.1039/c4ra16721j
38. J. Fu, S. Qu, J.H. Ding et al., Comparison of the microstructure, mechanical properties and distortion of stainless steel 316 L fabricated by micro and conventional laser powder bed fusion. Addit. Manuf. **44**, 102067 (2021). https://doi.org/10.1016/j.addma.2021.102067
39. Y.D. Jing, X.W. Fang, N.Y. Xi et al., Investigation of microstructure and mechanical properties evolution in 7050 aluminum alloy and 316L stainless steel treated by laser shock peening. Mater. Charact. **182**, 111571 (2021). https://doi.org/10.1016/j.matchar.2021.111571
40. X. Li, X. Fang, X. Jiang et al., Additively manufactured high-performance AZ91D magnesium alloys with excellent strength and ductility via nanoparticles reinforcement. Addit. Manuf. **69**, 103550 (2023). https://doi.org/10.1016/j.addma.2023.103550
41. J.E. Bailey, P.B. Hirsch, The dislocation distribution, flow stress, and stored energy in cold-worked polycrystalline silver. Phil. Mag. **5**, 485–497 (1960). https://doi.org/10.1080/14786436008238300
42. P. Deng, M. Karadge, R.B. Rebak et al., The origin and formation of oxygen inclusions in austenitic stainless steels manufactured by laser powder bed fusion. Addit. Manuf. **35**, 101334 (2020). https://doi.org/10.1016/j.addma.2020.101334
43. K. Huang, K. Marthinsen, Q.L. Zhao et al., The double-edge effect of second-phase particles on the recrystallization behaviour and associated mechanical properties of metallic materials. Prog. Mater Sci. **92**, 284–331 (2018). https://doi.org/10.1016/j.pmatsci.2017.10.004